A Hybrid Spectral/Finite Element Method for Accurate and Efficient Modelling of Crack-Induced Contact Acoustic Nonlinearity

Feilong Li, Fangxin Zou[1]

Interdisciplinary Division of Aeronautical and Aviation Engineering, the Hong Kong Polytechnic University, Hung Hom, Kowloon, Hong Kong SAR, China

Keywords: Finite element; Spectral element; Ultrasonic wave; Contact acoustic nonlinearity; Crack.

Abstract

We propose a 2D hybrid spectral/finite element scheme for numerically resolving crack-induced contact acoustic nonlinearity in solid structures. While the high-order spectral element method (SEM) is much more efficient than the classical low-order finite element method (FEM), the fact that spectral elements are relatively large renders the SEM ineffective in discretizing microscopic cracks. The classical FEM, on the other hand, is good at modelling complex geometries. However, the computation of large-scale structures by the classical FEM can be extremely expensive. In this work, the coupling between high-order spectral elements and low-order finite elements is formulated by the Lagrange multipliers method. The nonlinear contact between crack surfaces is modelled using a penalty method. The aim of the proposed hybrid method is to simultaneously reduce the degrees of freedom (DOFs) in systems and ensure high numerical accuracy. A comprehensive mesh convergence study has been conducted to demonstrate the high convergence rate of the proposed method in modelling ultrasonic wave propagation, and its capability to converge for weak crack-induced contact acoustic nonlinearity. Through a series of numerical experiments on generation and propagation of nonlinear ultrasonic wave modes, the proposed method has been shown to possess a high accuracy and geometric flexibility, and require significantly less computational resources than the classical FEM. The proposed hybrid method will provide an efficient, accurate and robust numerical approach for studying crack-induced contact acoustic nonlinearity which nowadays is being widely exploited by non-destructive testing applications.

1. Introduction

In the past several decades, ultrasonic non-destructive testing techniques have been widely employed to detect and monitor defects in engineering structures [1-3]. However, the fact that an ultrasonic wave would fail to reflect or scatter from a damage that is much smaller than its wavelength limits the accuracy and sensitivity of conventional, essentially linear, ultrasonic

---

[1] Corresponding author. Email: frank.zou@polyu.edu.hk

inspection techniques. Therefore, the evaluation of weak material degradations in structures has always been a really tough challenge. In this respect, researchers have put much effort into developing new ultrasonic inspection techniques and discovered that as long as certain conditions are satisfied, the interaction between an ultrasonic wave and a damage would generate detectable nonlinear ultrasonic wave modes, even if the size of the damage is much smaller than wavelength of the incident wave [4-6]. Such discoveries, which opened up the possibility of detecting weak early-stage defects in structures, have been extensively investigated in recent years, alongside the development of nonlinear ultrasonic inspection techniques.

Cracks represent one of the most common types of defects in real engineering structures. Their dynamics is fundamentally governed by contact mechanics which would introduce nonlinearity into structural systems [7-9]. When a dynamic external load is exerted onto a crack, the two crack surfaces would open and close. Owing to the difference between the tensile and the compression modulus around the crack, a nonlinear contact motion would be induced. It is this nonlinear contact mechanics that would generate nonlinear ultrasonic wave modes, such as high-order harmonic waves [10], sub-harmonic waves [11] and mixed resonant waves [12], when a crack is impinged by an incident ultrasonic wave. Research activities on the contact mechanics of cracks and the interactions between cracks and ultrasonic waves rely heavily on mathematical modelling. While it would be almost impossible to obtain the solutions of the nonlinear responses of large-scale, complex engineering structures analytically, numerical simulations are pervasively used due to their robustness, low cost and high accuracy. In this work, we are devoted to applying partial differential equations, which are usually solved by the finite element method (FEM) [13], to numerically approximate nonlinear contact acoustic problems.

The FEM has been widely used to solve ultrasonic wave propagation problems [13, 14]. However, the standard low-order FEM is not very efficient in addressing these problems [13, 15] due to the dispersion and dissipation errors [16, 17] that would arise from elongations of numerical simulation time periods and attenuations of wave amplitudes [13]. Such errors would accumulate as a wave propagates further. It is acknowledged that in order to reduce these errors and extract accurate solutions, very fine meshes are usually adopted, especially for problems that deal with large wavenumbers [13, 18]. Therefore, to model a large structure using the standard FEM, a huge number of elements would be required, resulting in an enormous computational cost.

Compared with the standard FEM, the spectral element method (SEM), which is essentially a high-order FEM, is more accurate and converges much more quickly [19, 20]. The SEM is able to simulate ultrasonic wave propagation much more efficiently using fewer elements and hence less computational resource [21]. In using the SEM, deformations are approximated by high-order polynomials such as the Lobatto polynomials, the Chebyshev polynomials and the Laguerre polynomials [22]. The nodal arrangement of a discretized high-order spectral element (SE) is related to the type of the interpolating polynomials used. For instance, for elements whose deformations are approximated by the Lobatto polynomials, their nodes could be defined by the Gauss-Lobatto-Legendre (GLL) quadrature points [23]. The SEM was first introduced by Patera

in fluid dynamics [20]. It has since been used to model both linear [24] and nonlinear [25] elastic wave propagation in solid structures. Also, a 3D SEM for simulating ultrasonic inspection of defects in plate structures has been proposed by Peng et al. [23]. Recently, GPU-enabled parallel implementation of a 3D SEM for wave propagation problems was introduced and a significant improvement in computational speed was achieved [26, 27].

Consider a domain with microscopic geometric features such as small cracks or holes. Pure SEM, which uses relatively large elements, could be inaccurate in describing the geometries of the micro-features. The standard FEM, on the other hand, would decompose the micro-features more precisely. However, if the remaining regularly structured regions of the domain are also modelled by low-order finite elements (FEs), the simulation of ultrasonic wave propagation would be extremely expensive. Therefore, the most ideal approach would be to discretize the regularly structured regions of the domain into high-order SEs and the regions containing the micro-features into low-order FEs. In this work, a 2D hybrid SEM/FEM approach for numerically approximating the generation and propagation of crack-induced nonlinear ultrasonic wave modes in solid structures is proposed.

To couple a SE mesh and a FE mesh, tie constraints are applied at their interface through the Lagrange multipliers method [28, 29], which does not introduce nonlinearity into the system. Similar hybrid formulations have been proposed for earthquake wave simulations [30] and fluid-structure interaction problems [31]. For dealing with the interfaces of non-matching meshes, the mortar method has been shown to possess a high accuracy and stability [32]. Bernardi et al. tied linear FEs to SEs using the mortar method to handle solid mechanics problems [33]. Zuchowski et al. employed the mortar method in simulating soil-structure interactions [34]. However, to the best of the authors' knowledge, there has not been a hybrid SEM/FEM approach for modelling contact acoustic nonlinearity.

It is worth mentioning that there are also some other alternatives for coupling multiple domains. For instance, adhesive layers that are modelled by 2D shell elements were used to bond 3D piezoelectric transducers to 3D composite plates, both of which are discretized by SEs [35]. A compatible transition element, the xNy-element, was proposed to couple elements that differ in element size, shape function type or polynomial order [36]. Bridging subdomains were employed to connect macroscopic continuum domains to microscopic molecular domains [37]. To link a FE domain with a boundary element domain, a common subdomain that is formulated by both the FEM and the boundary element method could be used [38]. What's more, the extended finite element method could realize local mesh enrichment to model the behaviors of cracks without resorting to introducing a fine local mesh and coupling it with the coarse background mesh [39].

This paper is organized as follows. Section 2 describes the problem that we intended to solve. Two tasks, namely tying SE and FE meshes and modelling the nonlinear contact between crack surfaces, were addressed by the Lagrange multipliers method [28] and a penalty method [40] respectively. The explicit time integration scheme for the nonlinear dynamics concerned is also discussed. In Section 3, mesh convergence studies for the standard FEM, pure SEM and the hybrid

approach are firstly presented. Here, the standard FEM was executed by the inhouse code in Fortran language. Then, three numerical examples, namely the crack-induced generation of the second harmonic mode of longitudinal waves, the collinear mixing of Lamb waves, and the non-collinear mixing of bulk waves, were computed using the hybrid approach. The results obtained were compared to those computed by the standard FEM. What different from the convergence studies is that the standard FEM for those three examples is executed by the commercial software package ABAQUS® [41] instead. The paper is concluded in Section 4.

2. Problem Description

Consider a 2D bounded medium $\Omega \subset \square^2$ as illustrated in **Fig. 1**. Ω is divided into two subdomains Ω_1 and Ω_2 with boundaries $\partial\Omega_1$ and $\partial\Omega_2$, and satisfies two conditions: $\Omega_1 \cap \Omega_2 = \varnothing$ and $\partial\Omega_1 \cap \partial\Omega_2 = \gamma$, where γ represents the interface between the two subdomains. The regularly structured subdomain Ω_1 is discretized into SEs, and Ω_2, which contains a small crack, into low-order quadrilateral FEs. The SE subdomain is assigned linear elastic material properties since the deformations associated with ultrasonic wave propagation are small. The use of linear elastic material properties would help to reduce the computational cost because the global stiffness matrix of the subdomain would only need to be constructed once. The FE subdomain, on the other hand, adapts well to the locally complex geometry incurred by the presence of the crack. Also, it has been shown that the standard FEM copes well with the nonlinear contact between crack surfaces [42-44].
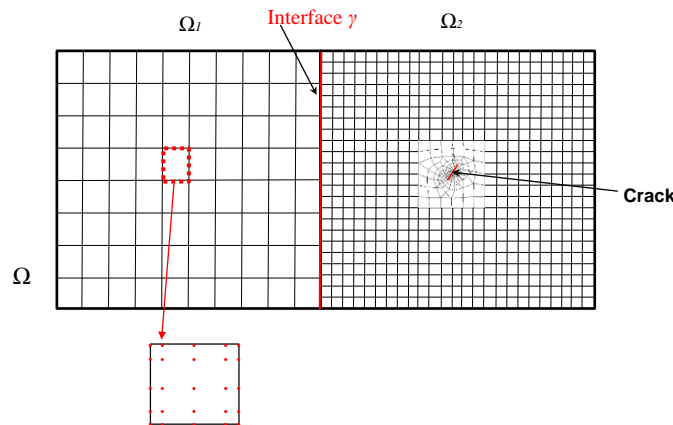

Fig. 1. Coupling of a FE and a SE subdomain.

In this work, the SEs used adopt the Gauss-Lobatto-Legendre (GLL) quadrature points as nodes and the Lagrange polynomials as shape functions. For both SE and FE subdomains, the Gauss–Legendre quadrature is employed to compute stiffness matrices. In comparison, mass matrices are computed by the GLL quadrature and are therefore diagonal. Diagonal mass matrices are optimal for explicit time integration.

4

Considering the coupling of the two subdomains (solved by the Lagrange multipliers method [28]) and the nonlinear contact between the two crack surfaces (solved by a penalty method [40]), the dynamics of the bounded medium Ω can be described by

$$\mathbf{Ma}(t) + \mathbf{F}_{int}(\mathbf{u}(t)) + \mathbf{F}_c + \mathbf{G}\lambda = \mathbf{F}_{ext}(t) \tag{1}$$

and

$$\mathbf{G}^T \mathbf{v} = \mathbf{0} \tag{2}$$

where $\mathbf{u}$, $\mathbf{v}$ and $\mathbf{a}$ denote the displacements, the velocities, and the accelerations of the medium respectively, t: time, $\mathbf{M}$: the mass matrix, $\mathbf{F}_{int}$: the internal forces (which can be expressed in terms the stiffness matrix and the displacements), $\mathbf{F}_c$: the contact forces on the crack surfaces, $\mathbf{F}_{ext}$: the external loads, $\mathbf{G}$: the constraint matrix for coupling the SE and the SE subdomains, λ: the Lagrange multipliers. Using a semi-discrete approach, approximate solutions of Eq. (1) can be found by applying a temporal discretization scheme, which will be explained in Section 2.3. Eq. (2) represents the coupling of the deformations along the two boundaries of the mesh tying interface. While the detailed derivation of Eq. (2) will be shown in Section 2.1, it is worth mentioning here that constraining velocities, as done by Eq. (2), is equivalent to constraining displacements, since the two boundaries share the same initial conditions.

Eq. (1) could be highly nonlinear, depending on $\mathbf{F}_{int}$ and $\mathbf{F}_c$. $\mathbf{F}_{int}$ would become nonlinear if geometric or material nonlinearities, which would complicate the displacement vector and the stiffness matrix, are taken into account. $\mathbf{F}_c$ would be introduced into the system if nonlinear contact, such as frictional or frictionless collisions, takes place. In this work, we only consider the nonlinear contact between crack surfaces, assuming that the two surfaces of a crack are frictionless and would flap under a dynamic load. The contact mechanics is approximated by a penalty method which can deal with the dynamic contact in a direct manner and does not need to introduce additional degrees of freedom (DOFs) into systems.

It is worth mentioning that neither the constraint forces $\mathbf{G}\lambda$ nor the mesh tying constraints $\mathbf{G}^T \mathbf{v} = \mathbf{0}$ would introduce additional nonlinearity into the system. This is due to the fact that in a mesh tying problem, the boundaries of the subdomains are not permitted to move relative to each other, different from a contact problem which actually allows the contact surfaces to slide and extrude each other, generating nonlinearity. With regards to computational efficiency, the computation of the mortar coupling constraint matrix $\mathbf{G}$, which is constant, is a one-off cost. The Lagrange multipliers in λ can be calculated through simple operations associated with the SE/FE interface, although they need to be updated at every time step. Therefore, the computational cost for tying non-matching meshes can usually be ignored compared with the global computational cost.

2.1.Surface-to-Surface Tie Constraint

In Eq. (1) which uses the Lagrange multipliers method [28, 32] to couple non-matching meshes, the terms in $\mathbf{G}\lambda$ can be seen as connecting forces. These terms are formed numerically by applying the surface-to-surface tie [32, 45], which has been shown to be efficient, stable and accurate for tying non-matching meshes, not only for flat interfaces, but also for curved non-conforming cases [46]. An example of SE/FE interfaces is shown in **Fig. 2**. The surface-to-surface tie on the interface is addressed by the classical master-slave strategy [7, 46-48], based on which side with the dense mesh, i.e. the boundary of the FE subdomain, is assigned the slave surface denoted by γ^1, and the boundary of the SE subdomain is set as master surface denoted by γ^2. In addition, selecting the boundary of the SE subdomain as the master surface would lead to a higher accuracy because the deformations of SEs are approximated by high-order shape functions. In this work, master and slave surfaces are always flat lines. Every pair of master and slave surfaces share a geometrically unanimous interface.
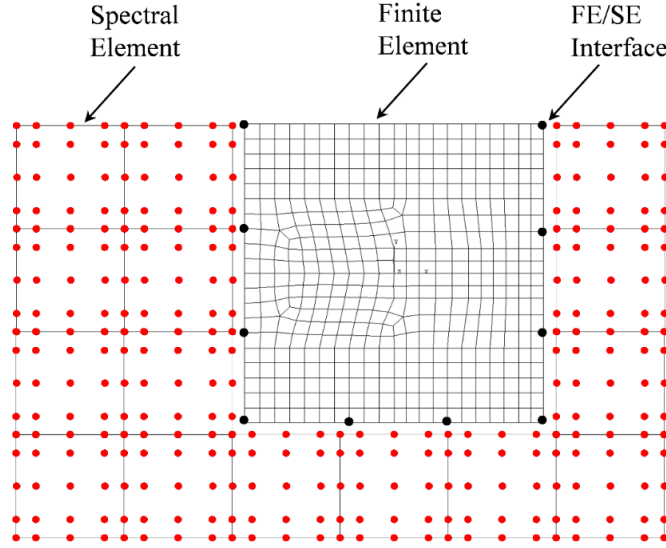

Fig. 2. Schematic of the coupling between SEs and FEs.

We consider the displacement continuity along the SE/FE interface γ as

$$\int_\gamma (\mathbf{u}^{FE} - \mathbf{u}^{SE}) \cdot \mathbf{N}_i = 0, \quad \forall i = 1,\ldots,N_\gamma^{FE} \tag{3}$$

where $\mathbf{N}_i$ contains the shape functions associated with the ith FE node and the corresponding SE node on the interface, and N_γ^{FE} is the number of FE nodes on the interface. In order to ensure good stability and simplicity in the time integration process, the displacement continuity conditions are replaced by identical velocity continuity conditions as follows

$$\int_\gamma (\mathbf{v}^{FE} - \mathbf{v}^{SE}) \cdot \mathbf{N}_i = 0, \quad \forall i = 1, \dots, N_\gamma^{FE} \tag{4}$$

In fact, Eq. (4) is fully equivalent to Eq. (3) because it is obtainable by differentiating Eq. (3) with respect to time. For the initial conditions, the velocities and the displacements of the system at $t = 0$ are set to 0. Therefore, the displacement and the velocity continuity conditions are satisfied and the compatibility conditions on the interface are automatically ensured. Compared with displacement continuity conditions, velocity continuity conditions can be naturally implemented in the standard time integration scheme. The following section will show the procedure for imposing tie constraints onto the interface.

Considering only the coupling between SEs and FEs which is realized by the Lagrange multipliers method, Eq. (1) and Eq. (4) can be rewritten as

$$\mathbf{Ma} = \mathbf{F}_{ext} + \mathbf{F}_{int} + \mathbf{G}\lambda \tag{5}$$

and

$$\mathbf{G}^T\mathbf{v} = \mathbf{0} \tag{6}$$

It is worth mentioning that Eq. (6) is general to the whole system, but in the constrain matrix $\mathbf{G}$, only the terms that correspond to the SE/FE interface are non-zero. In applying tie constraints on the interface, master-slave node pairs are searched and established prior to the dynamic analysis, and remain invariant throughout the analysis, making the constraint matrix $\mathbf{G}$ constant. $\mathbf{G}$ is formed based on the shape functions of the SEs and the FEs used [49]. By multiplying both sides of Eq. (5) by $\mathbf{G}^T\mathbf{M}^{-1}$, the following expression is obtained

$$\mathbf{G}^T\mathbf{M}^{-1}\mathbf{G}\lambda = \mathbf{G}^T\mathbf{a} - \mathbf{G}^T\mathbf{M}^{-1}(\mathbf{F}_{ext} + \mathbf{F}_{int}) \tag{7}$$

In our work, the velocity Verlet method [50], which is one type of central difference methods, is adopted. The mid-step velocity at the nth time step is given by

$$\mathbf{v}^{n+1/2} = \mathbf{v}^n + \frac{\Delta t}{2}\mathbf{a}^n \tag{8}$$

where the acceleration and the velocity at the nth time step can be computed using the standard time integration scheme. Then, we can calculate the velocity at the $(n+1)^{th}$ time step by

$$\mathbf{v}^{n+1} = \mathbf{v}^{n+1/2} + \frac{\Delta t}{2}\mathbf{a}^{n+1} \tag{9}$$

By rearranging Eq. (9) and multiplying both sides of the equation by $\mathbf{G}^T$, we obtain

7

$$\mathbf{G}^{\mathrm{T}}\mathbf{a}^{n+1} = \frac{2}{\Delta t}\mathbf{G}^{\mathrm{T}}(\mathbf{v}^{n+1} - \mathbf{v}^{n+1/2}) \tag{10}$$

By substituting Eq. (10) into Eq. (7) and imposing the tie constraints governed by Eq. (6), we get

$$\mathbf{G}^{\mathrm{T}}\mathbf{M}^{-1}\mathbf{G}\boldsymbol{\lambda} = -\frac{2}{\Delta t}\mathbf{G}^{\mathrm{T}}\mathbf{v}^{n+1/2} - \mathbf{G}^{\mathrm{T}}\mathbf{M}^{-1}(\mathbf{F}_{\mathrm{ext}} + \mathbf{F}_{\mathrm{int}}) \tag{11}$$

In Eq. (11), $\mathbf{F}_{\mathrm{int}}$ can be evaluated based on the stiffness matrix and the displacements at the $(n+1)^{th}$ time step. Eq. (11) is finally converted into the classical format of $\mathbf{Ax} = \mathbf{b}$ to be solved numerically for λ. Once λ has been obtained, we can compute the constraint forces $\mathbf{G}\boldsymbol{\lambda}$, the accelerations at the next time step using Eq. (5), and the velocities at the next time step using Eq. (8) and Eq. (9). The details of the time integration process will be further elaborated in Section 2.3.

2.2. Dynamic Contact Nonlinearity

We also use the classical master-slave strategy to deal with the dynamic contact mechanics of crack surfaces [51]. Generally speaking, it is assumed that the two surfaces of a crack are allowed to slide and separate but, under the small deformation condition, cannot penetrate each other. The key process for solving a contact problem is pairing up contact nodes and resisting penetrations into the contact surfaces at every time step. This section describes the regularization of the non-penetration condition using a penalty method.

2.2.1. Contact Kinematics

For a 2D contact problem as illustrated in **Fig. 3**, a point **S** with a local Gaussian coordinate of ξ^1 is firstly defined on the slave surface. The closest point **M** on the master surface is then found by closest point projection [52]. $\boldsymbol{\rho}$ and $\mathbf{r}$ are, respectively, the position vectors of **S** and **M** in the global coordinate system. Based on $\boldsymbol{\rho}$ and $\mathbf{r}$, the normal vector **n** of the contact interface can be obtained. The contact motion ξ^3 of the two surfaces is governed by

$$\mathbf{r}(\xi^1, \xi^3) = \boldsymbol{\rho}(\xi^1) + \xi^3 \mathbf{n} \tag{12}$$

Since the master surface is also parametrized by the local Gaussian coordinate system, $\boldsymbol{\rho}$ can be essentially expressed as a function of ξ^1. The exact contact situation is determined according to Eq. (13), based on the value of ξ^3. If contact occurs, the non-penetration condition will need to be applied to the system.

$$\xi^3 \begin{cases} > 0, \text{ no contact.} \\ = 0, \text{ contact without penetration.} \\ < 0, \text{ contact with penetration.} \end{cases} \tag{13}$$
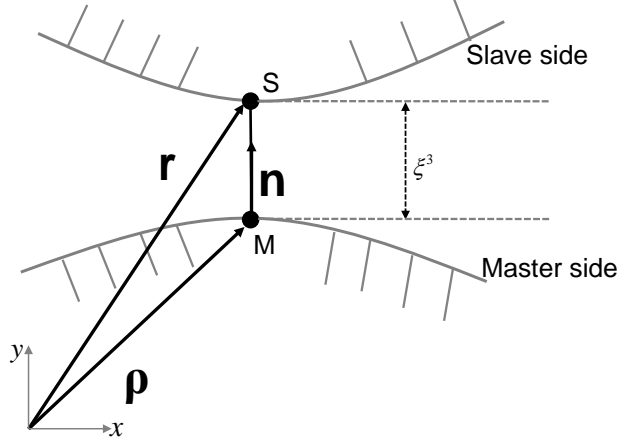
Fig. 3. Kinematics for a 2D contact problem.

2.2.2. Weak Formulation

When contact occurs, the contact traction on the contact point should be considered. As shown in **Fig. 4**, s_A and s_B denote the lengths of the two contact surfaces, ds_A and ds_B two infinitesimally small segments of the contact surfaces, where $ds_A = ds_B$, and $\mathbf{R}_A$ and $\mathbf{R}_B$ the contact force vectors on the contact surfaces. Assuming that $\mathbf{R}_A$ and $\mathbf{R}_B$ result in two virtual displacements $\delta\mathbf{u}_A$ and $\delta\mathbf{u}_B$, the virtual work δW^c is obtained by the following integrals over the contact surfaces

$$\delta W^c = \int_{s_A} \mathbf{R}_A \cdot \delta\mathbf{u}_A ds_A + \int_{s_B} \mathbf{R}_B \cdot \delta\mathbf{u}_B ds_B \tag{14}$$

The contact forces can be regarded as either internal or external forces and have to be added to the global system. The local equilibrium of the contact interface is governed by

$$\mathbf{R}_A \cdot ds_A + \mathbf{R}_B \cdot ds_B = \mathbf{0} \tag{15}$$

Based on Eq. (15), Eq. (14) can be transformed into an integral over only one contact surface, either the master surface *A* or the slave surface *B*. In the latter case, Eq. (14) becomes

$$\delta W^c = \int_{s_B} \mathbf{R}_B \cdot (\delta\mathbf{u}_B - \delta\mathbf{u}_A) ds_B \tag{16}$$

By expressing the contact interface by *s* and the contact traction by $\mathbf{R}$, Eq. (16) can be rewritten as

$$\delta W^c = \int_s \mathbf{R} \cdot (\delta\mathbf{u}_B - \delta\mathbf{u}_A) ds \tag{17}$$

In this work, the contact considered is frictionless. Therefore, $\mathbf{R}$ in Eq. (17) contains only the normal traction and is given by

$$\mathbf{R} = N\mathbf{n} \tag{18}$$

The variation of displacements $\delta\mathbf{u}_B - \delta\mathbf{u}_A$ is fully equivalent to the variation of positions $\delta\mathbf{r} - \delta\boldsymbol{\rho}$. By rearranging Eq. (12) and carrying out partial differentiation, the variation of displacements can be expressed as

$$\delta\mathbf{u}_B - \delta\mathbf{u}_A = \delta\mathbf{r} - \delta\boldsymbol{\rho} = \frac{d\boldsymbol{\rho}}{d\xi^1}\dot{\xi}^1 + \mathbf{n}\delta\xi^3 + \xi^3\frac{d\mathbf{n}}{dt} \tag{19}$$

During contact, penetrations into contact surfaces are not allowed, leading to $\xi^3 = 0$. Therefore, Eq. (19) becomes

$$\delta\mathbf{u}_B - \delta\mathbf{u}_A = \delta\mathbf{r} - \delta\boldsymbol{\rho} = \frac{d\boldsymbol{\rho}}{d\xi^1}\delta\xi^1 + \mathbf{n}\delta\xi^3 \tag{20}$$

Note that $d\boldsymbol{\rho}/d\xi^1$ is the tangent vector of the master surface and fulfills the conditions $\mathbf{R} \perp d\boldsymbol{\rho}/d\xi^1$. By substituting Eq. (20) into Eq. (17), the virtual work of the contact traction can be rewritten as

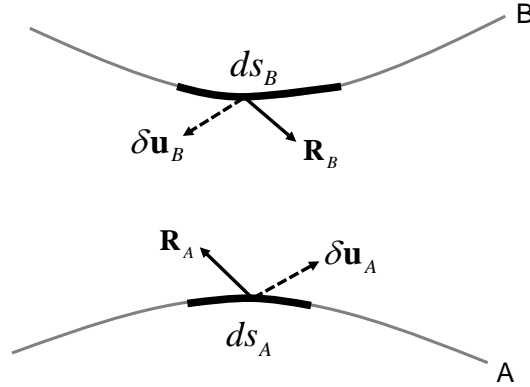$$\delta W^c = \int_s N\delta\xi^3 ds \tag{21}$$

Fig. 4. Equilibrium condition for a 2D contact problem.

2.2.3. Regularization by a Penalty Method

Contact tractions are usually unknown and need to be computed first. In view of this, a penalty method is used to calculate contact tractions by constructing a new functional without introducing additional unknowns. By penalty regularization, the frictionless contact traction N in Eq. (21) can be written as

$$N = \varepsilon_N H(-\xi^3)\xi^3 \quad \text{with} \quad H(-\xi^3) = \begin{cases} 0, & \xi^3 > 0 \\ 1, & \xi^3 \leq 0 \end{cases} \tag{22}$$

where ε_N is a penalty parameter and $H(-\xi^3)$ is a Heaviside function. Since penetrations are not allowed in this work, Eq. (22) essentially implies that if the two surfaces of a crack are in contact, a normal force will emerge to resist penetration. Using the regularization scheme, the virtual work given by Eq. (21) is transformed into the following expression

$$\delta W^c = \int_s \varepsilon_N H(-\xi^3)\xi^3 \delta\xi^3 ds \tag{23}$$

Eq. (23) provides the common energy formalism for contact problems. Its numerical solution process will be described in next two sections.

2.2.4. Numerical Discretization for Segment-To-Segment Approach

The segment-to-segment (STS) approach, also known as the surface-to-surface approach, is often used to model the contact mechanics of crack surfaces in numerical simulations. It is known to be more reliable and steadier than the node-to-surface approach [47, 51]. Consider a master and a slave surface that are discretized into quadrilateral elements. A contact segment pair of the contact interface is showed in **Fig. 5**. In order to establish the contact segment pair, the nodes on the master and the slave segments, i.e. M_1 and S_2, are projected onto the opposite surface as η_a and ξ_b^1, and the integration points on the slave segment, denoted by η_i, are projected onto the master segment as ξ_i^1.
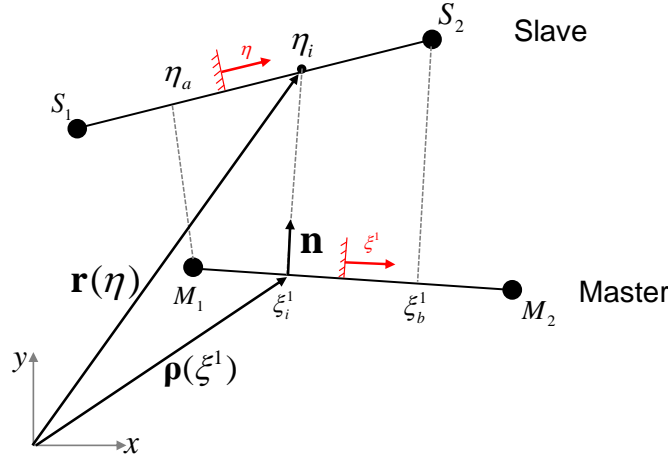

Fig. 5. Geometry and kinematics of a contact segment pair which is bounded by the points η_a, S_2, ξ_b^1 and M_1.

The virtual work given by Eq. (23) can be approximated by the following numerical integration over the slave segment

$$\delta W^c = \int_s \varepsilon_N H(-\xi^3)\xi^3(\xi^1)\delta\xi^3(\xi^1)ds(\eta)$$

$$= \sum_{i=1}^{N_{ipt}} \varepsilon_N H(-\xi^3)\xi^3(\xi_i^1)\delta\xi^3(\xi_i^1)\sqrt{\mathbf{r}_\eta \cdot \mathbf{r}_\eta}\Big|_{\eta_i} w_i \tag{24}$$

where N_{ipt} is number of integration points on the slave segment. In order to solve Eq. (24), the contact situations at the integration points on the slave segment need to be determined based on Eq. (13). If the penetration ξ^3 at a given integration point is found to be negative, the contact mechanics of the point will need to be considered. The computation of ξ^3 is discussed as follows.

The position vectors of the nodes of the elements that are involved in the contact segment pair can be expressed as

$$[\mathbf{x}] = \begin{bmatrix} x_M^{(1)} & y_M^{(1)} & x_M^{(2)} & y_M^{(2)} & x_S^{(1)} & y_S^{(1)} & x_S^{(2)} & y_S^{(2)} \end{bmatrix}^{\mathrm{T}} \tag{25}$$

where $\left(x_M^{(1)}\ y_M^{(1)}\right)$ and $\left(x_M^{(2)}\ y_M^{(2)}\right)$ are the Cartesian coordinates of nodes M_1 and M_2 on the master segment, and $\left(x_S^{(1)}\ y_S^{(1)}\right)$ and $\left(x_S^{(2)}\ y_S^{(2)}\right)$ the Cartesian coordinates of nodes S_1 and S_2 on the slave segment. Since the deformations of the master and the slave segments are approximated by the 1st-order Lagrange polynomials, the relative displacement of the contact segments can be calculated by

$$\mathbf{r}(\eta)-\boldsymbol{\rho}(\xi^1) = \begin{bmatrix} -N_1 & 0 & -N_2 & 0 & M_1 & 0 & M_2 & 0 \\ 0 & -N_1 & 0 & -N_2 & 0 & M_1 & 0 & M_2 \end{bmatrix} \begin{pmatrix} x_M^{(1)} \\ y_M^{(1)} \\ x_M^{(2)} \\ y_M^{(2)} \\ x_S^{(1)} \\ y_S^{(1)} \\ x_S^{(2)} \\ y_S^{(2)} \end{pmatrix} = [A(\xi^1,\eta)][\mathbf{x}] \tag{26}$$

where

$$[A(\xi^1,\eta)] = \begin{bmatrix} -\dfrac{1-\xi^1}{2} & 0 & -\dfrac{1+\xi^1}{2} & 0 & \dfrac{1-\eta}{2} & 0 & \dfrac{1+\eta}{2} & 0 \\ 0 & -\dfrac{1-\xi^1}{2} & 0 & -\dfrac{1+\xi^1}{2} & 0 & \dfrac{1-\eta}{2} & 0 & \dfrac{1+\eta}{2} \end{bmatrix} \tag{27}$$

12

The tangent vectors of the master and the slave surface, i.e. $\mathbf{\rho}_{\xi^1}$ and $\mathbf{r}_\eta$, are formulated as

$$\mathbf{\rho}_{\xi^1} = -[A_{\xi^1}][\mathbf{x}] \tag{28}$$

$$\mathbf{r}_\eta = -[A_\eta][\mathbf{x}] \tag{29}$$

where the derivatives of the matrix $[A(\xi^1, \eta)]$ are given by

$$[A_{\xi^1}] = \frac{\partial[A]}{\partial \xi^1} = \frac{1}{2}\begin{bmatrix} 1 & 0 & -1 & 0 & 0 & 0 & 0 & 0 \\ 0 & 1 & 0 & -1 & 0 & 0 & 0 & 0 \end{bmatrix} \tag{30}$$

$$[A_\eta] = \frac{\partial[A]}{\partial \eta} = \frac{1}{2}\begin{bmatrix} 0 & 0 & 0 & 0 & -1 & 0 & 1 & 0 \\ 0 & 0 & 0 & 0 & 0 & -1 & 0 & 1 \end{bmatrix} \tag{31}$$

The direction of the normal vector of the master segment $\mathbf{n}(\xi^1)$ is regulated as follows

$$\mathbf{n} = \mathbf{k} \times \mathbf{\tau} = \begin{vmatrix} i & j & k \\ 0 & 0 & 1 \\ x_M^{(2)} - x_M^{(1)} & y_M^{(2)} - y_M^{(1)} & 0 \end{vmatrix} \frac{1}{L} = \frac{1}{L}\begin{bmatrix} y_M^{(1)} - y_M^{(2)} \\ x_M^{(2)} - x_M^{(1)} \end{bmatrix} \tag{32}$$

where $L = \sqrt{(x_M^{(2)} - x_M^{(1)})^2 + (y_M^{(2)} - y_M^{(1)})^2}$, $\mathbf{\tau}$ is the tangent vector along the contact interface, $\mathbf{k}$ is the unit vector along the z-direction in the Cartesian coordinate system. Since the normal vector $\mathbf{n}$ points outwards from the master segment, the contact motion can be calculated by

$$\xi^3 = (\mathbf{r}(\eta) - \mathbf{\rho}(\xi^1))^{\mathrm{T}} \cdot \mathbf{n} = [\mathbf{x}]^{\mathrm{T}}[A]^{\mathrm{T}}\mathbf{n} \tag{33}$$

After ξ^3 has been obtained, the contact situation can be determined.

2.2.5. Residual and Tangent Matrix

The STS contact algorithm is executed by the discretization of Eq. (24) as

$$\begin{aligned} \delta W^c &= \sum_{i=1}^{N_{ipt}} \varepsilon_N H(-\xi^3)\xi^3 (\delta\mathbf{r}(\eta) - \delta\mathbf{\rho}(\xi^1))^{\mathrm{T}} \cdot \mathbf{n}\sqrt{\mathbf{r}_\eta \cdot \mathbf{r}_\eta}\, w_i \\ &= \sum_{i=1}^{N_{ipt}} \varepsilon_N H(-\xi^3)\xi^3 \delta[\mathbf{x}]^{\mathrm{T}}[A(\xi^1, \eta)]^{\mathrm{T}} \cdot \mathbf{n}\sqrt{\mathbf{r}_\eta \cdot \mathbf{r}_\eta}\, w_i \end{aligned} \tag{34}$$

The linearization of Eq. (34) [51, 53] leads to the residual

13

$$\mathbf{R} = \sum_{i=1}^{k} \varepsilon_N H(-\xi^3) \xi^3 [A]^{\mathrm{T}} \cdot \mathbf{n} \sqrt{\mathbf{r}_\eta \cdot \mathbf{r}_\eta} \, w_i \tag{35}$$

and the tangent matrix

$$[K] = \sum_{i=1}^{k} \varepsilon_N H(-\xi^3) \{ [A]^{\mathrm{T}} \mathbf{n} \otimes \mathbf{n}[A] - \xi^3 m^{11} ([A_{\xi^1}]^{\mathrm{T}} \mathbf{n} \otimes \boldsymbol{\rho}_{\xi^1} [A] + [A]^{\mathrm{T}} \boldsymbol{\rho}_{\xi^1} \otimes \mathbf{n}[A_{\xi^1}]) \sqrt{\mathbf{r}_\eta \cdot \mathbf{r}_\eta} \, w_i \} \tag{36}$$

where $m^{11} = 1/(\boldsymbol{\rho}_{\xi^1} \cdot \boldsymbol{\rho}_{\xi^1})$. Here, we define the following regulation

$$\mathbf{a} \otimes \mathbf{b} = \begin{bmatrix} a_1 b_1 & a_1 b_2 \\ a_2 b_1 & a_2 b_2 \end{bmatrix} \tag{37}$$

where $\mathbf{a} = [a_1, a_2]$ and $\mathbf{b} = [b_1, b_2]$. In explicit time integration processes, residuals and tangent matrices are used to compute contact forces $\mathbf{F}_c$ which are added into global systems.

2.3. Explicit Time Integration

The explicit time integration algorithm for a linear elastic material requires

$$\Delta t \le \frac{h}{c_{mas}} \tag{38}$$

where h is a characteristic length of the mesh used, usually the shortest distance between two nodes, and c_{mas} is the maximum wave speed in the material. However, for systems that involve nonlinear contact between crack surfaces, Eq. (38) may become inapplicable because the dynamic motions of cracks could lead to complex deformations of crack surfaces. Also, it could be foreseen that the stable time steps would need be much smaller in order to ensure computational stability and numerical accuracy. Therefore, in this work, the stable time steps for the nonlinear systems were carefully determined through convergence studies, i.e., for a given system, the time step was gradually decreased until the solution had converged.

In this work, we adopt lumped mass matrices. On the other hand, a full integration scheme based on the Gauss–Legendre quadrature is applied to construct stiffness matrices. Because the constraint forces at SE/FE interfaces and the contact forces at crack nodes are not known initially, Eq. (1) is solved explicitly using the velocity Verlet method, the detail of which is shown below.

a) Initially calculation
    i) Form the stiffness matrix $\mathbf{K}$ and the mass matrix $\mathbf{M}$.
    ii) Define initial conditions $\mathbf{u}^0$, $\mathbf{v}^0$, and $\mathbf{a}^0$.
b) For every time step
    i) Calculate the mid-step velocity vector at time $t + \Delta t / 2$ using $\mathbf{v}^{n+1/2} = \mathbf{v}^n + \Delta t \mathbf{a}^n / 2$.

14

ii) Calculate the displacement vector at time $t + \Delta t$ using $\mathbf{u}^{n+1} = \mathbf{u}^n + \Delta t \mathbf{v}^{n+1/2}$.

iii) Calculate the internal force vector at time $t + \Delta t$ using $\mathbf{F}_{int} = \mathbf{K}\mathbf{u}^{n+1}$.

iv) Calculate the constraint forces $\mathbf{G}\lambda_{n+1}$ using Eq. (11).

v) Calculate the contact stiffness $[K]$ and the residual $\mathbf{R}$ at time $t + \Delta t$ using Eq. (35) and Eq. (36) respectively, and compute contact forces using $\mathbf{F}_c = -\mathbf{R} + [K]\mathbf{u}^{n+1}$.

vi) Update the acceleration at time $t + \Delta t$ using $\mathbf{a}^{n+1} = (\mathbf{F}_{ext} - \mathbf{F}_{int} + \mathbf{G}\lambda_{n+1} + \mathbf{F}_c)/\mathbf{M}$.

vii) Update velocity at time $t + \Delta t$ using $\mathbf{v}^{n+1} = \mathbf{v}^{n+1/2} + \Delta t \mathbf{a}^{n+1}/2$.

viii) Move onto the next time step.

3. Numerical Results

In this work, we adopt 25-node GLL elements for SEs and 4-node quadrilateral elements for FEs. For the mesh convergence studies presented in Section 3.1, both the hybrid SE/FE models and the standard FE models were executed by an inhouse Fortran code. In Sections 3.2 – 3.4, the generation and propagation of various nonlinear ultrasonic wave modes in structures with frictionless cracks will be simulated using the proposed hybrid FEM/SEM approach. In doing these numerical examples, the standard FE models, which were used for benchmark purpose, were executed by ABAQUS®, adopting CPE4R elements [41] and reduced integration for constructing stiffness matrices. In contrast, the stiffness matrices of the hybrid SE/FE models, which were implemented by the inhouse Fortran code, were constructed by full integration.

3.1. Mesh Convergence Studies

Convergence is the prerequisite for obtaining accurate numerical solutions as without it, approximation errors would arise. Convergence depends on several factors which include element type, element size and time increment. In this section, we examine the mesh convergence of the proposed hybrid approach, which is determined by the sizes of the elements used. It is known that the denser the mesh of a system is, the higher the accuracy would be. Nevertheless, the use of a dense mesh would increase computational cost. Therefore, when it comes to constructing a mesh, we would aim to strike a balance between numerical accuracy and computational cost. In this work, the mesh convergence criterion was set to when the difference between the solutions obtained by two consecutively sized meshes falls below 2%.

3.1.1. Mesh Convergence for 2D Linear Elastic Structures

First of all, we carried out mesh convergence studies for the 25-node GLL element based SEM and the 4-node quadrilateral element based FEM, using a 22.5 mm × 6 mm 2D linear elastic structure as shown in **Fig. 6**. The structure was assigned with a Young's modulus of 70 GPa, a Poisson's ratio of 0.33 and a density of 2700 kg·m^{-3}. A dynamic force excitation – $F(t) = A_0 \sin(2\pi f t) \times \sin(\pi f t/10)^2$, where $A_0 = 5$ MPa and $f = 1$ MHz are the peak amplitude and the central frequency – was imposed at one end of the structure. The top and the bottom boundaries of the structure were constrained to move simultaneously in the y-direction such that

the vibration of the particles in the structure in the y-direction was eliminated and only the vibration in the x-direction was allowed, resulting in the 1D longitudinal waves that were polarized in the x-direction and propagated in the x-direction. Displacements in the x-direction were acquired at the other end of the structure. To ensure the accuracies and efficiencies of the simulations, for each model, the stable time increment was chosen according to the time that the stress waves generated require to propagate through the smallest distance between two nodes in the densest mesh examined. As such, the stable time increment for the FE simulations was set to 1 ns and that for the SE simulations was set to 30 ns.
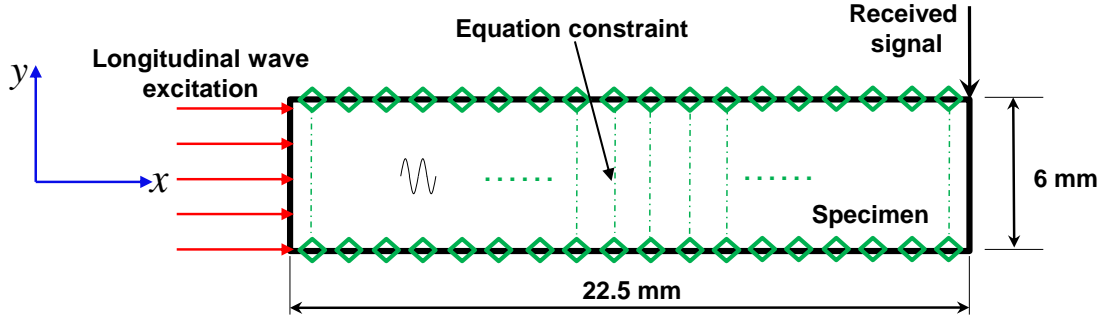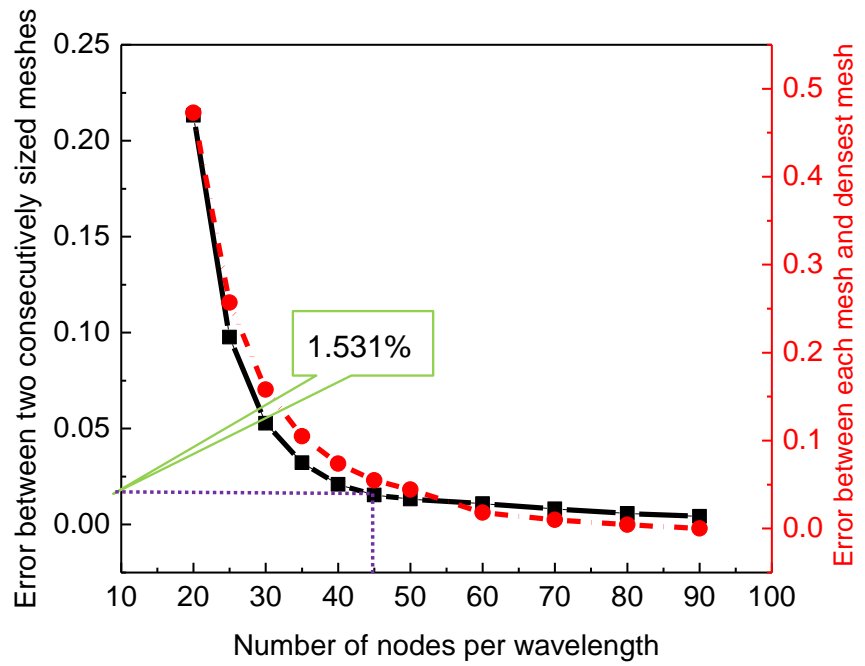

Fig. 6. Schematic diagram of an intact aluminium structure that allows for the propagation of 1D longitudinal waves.

The results of the mesh convergence studies are shown in **Fig. 7**. Here, the error between two consecutively sized meshes is defined by $error = \|\mathbf{u} - \mathbf{u}_0\| / \|\mathbf{u}_0\|$, where the vector $\mathbf{u}$ for each mesh contains the x-direction displacement of the right end of the structure at every time step, obtained by averaging the x-direction displacements of all the nodes on the right end of the structure, and the L^1 norm was used. As expected, for both the FE and the SE models, the error decreases when the number of nodes per wavelength increases. Notably, the SE model attains mesh convergence extremely fast at only 9 nodes per wavelength, with the error reaching as low as 0.0824%. Also, even if the number of nodes per wavelength is doubled to 18, the error does not further improve, confirming the validity of the mesh convergence at 9 nodes per wavelength. The FE model, on the other hand, requires 45 nodes per wavelength to reach mesh convergence. It can be seen that the accuracy of the FE model is lower than that of the SE model, and doubling the number of nodes per wavelength does not seem to help significantly. Moreover, for both models, the error between each of the meshes used and the densest mesh used was calculated by $error = \|\mathbf{u} - \mathbf{u}_r\| / \|\mathbf{u}_r\|$, where $\mathbf{u}_r$ is the solution computed by the densest mesh. The corresponding curves displayed in **Fig. 7** further prove the higher accuracy and the higher mesh convergence rate of the SE model. The results clearly demonstrate the potential of using the SEM to handle large-scale applications, which is also well shown in many other works.

(a)

(b)

17

3.1.2. Mesh Convergence for a Cracked Structure

In this work, dense FE meshes are used for regions containing cracks to guarantee the accuracy of nonlinear contact. Regularly structured regions that are far away from cracks are discretized into SEs. The intensities of the weak nonlinear ultrasonic wave modes that a crack induces upon interaction with an incident ultrasonic wave are often quantitively related to the characteristics of the crack. Therefore, nonlinear parameters, which are written in terms of the amplitudes of both the fundamental and the nonlinear wave modes, are introduced to quantitively characterize cracks. Different nonlinear parameters are used for different nonlinear wave modes. For second harmonic waves [54-56], the nonlinear parameters $\beta = A_2 / (A_1 A_1)$ and $\beta = A_2 / A_1$ are used to quantify classical material nonlinearity [55, 57] and contact nonlinearity [58] respectively, where A_1 and A_2 are the amplitudes of the fundamental and the second harmonic wave mode. In this work, only contact nonlinearity is concerned.

Fig. 8. shows a 100 mm $\times$ 3 mm 2D aluminum structure containing a vertical 0.5 mm long crack. The structure was decomposed into a SE and a FE region which are coupled via a straight interface. The crack is located in the center of FE region. The material properties and the boundary conditions of the structure are the same as those of the structure shown in **Fig. 6**. What were acquired as sensor signals are also the x-direction displacements of the right end of the structure.
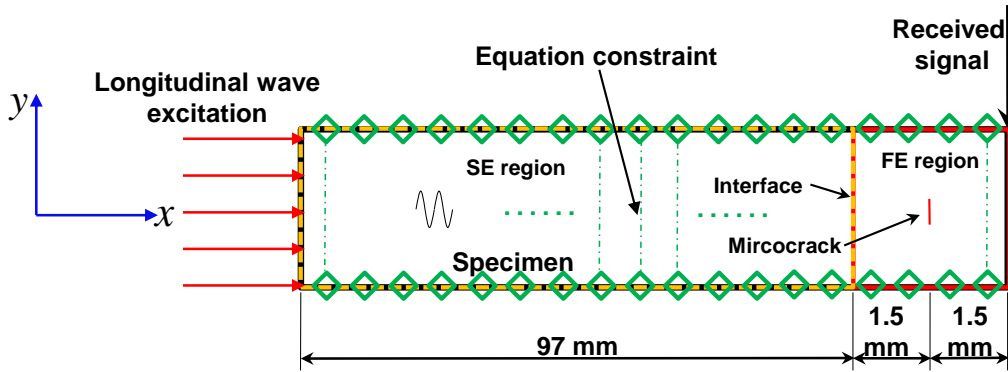

Fig. 8. Schematic diagram of the hybrid SE/FE model of a cracked aluminium structure that allows for the propagation of 1D longitudinal waves.

We examined the mesh convergence of the hybrid SE/FE model of the cracked structure with respect to the fundamental and the second harmonic modes of longitudinal waves. The mesh convergence of the standard FE model of the structure was also examined for benchmarking purpose. To ensure accurate simulations of the weak crack-induced contact acoustic nonlinearity, the stable time increment was set to 0.1 ns. Throughout the mesh convergence study, the size of the SEs in the hybrid model was set based on the mesh convergence criterion obtained in Section 3.1.1 and remained unchanged. What was gradually decreased, for both the hybrid model and the

standard FE model, is the size of the FEs, because the number of nodes required to converge the nonlinear contact of crack surfaces far exceeded the requirement for converging wave propagation. The convergence of the nonlinear contact of the crack surfaces was determined based on the error between two consecutively sized meshes, denoted by $error = \|\beta - \beta_0\| / \|\beta_0\|$, where the nonlinear parameter $\beta = A_2 / A_1$ could be calculated from the sensor signals acquired.

As illustrated in **Fig. 9**, for both the hybrid model and the standard FE model, the error between two consecutively sized meshes, by and large, drops with an increase in the number of the nodes used to partition the crack, though some fluctuations occur. For either model, the error becomes stable when the number of nodes on the crack is larger than 10. The number of nodes on the crack was further doubled to 20 to confirm the mesh convergence. The error was found to be almost unchanged. Furthermore, for both models, the error between each of the meshes used and the densest mesh used was calculated by $error = \|\beta - \beta_r\| / \|\beta_r\|$, where β_r is the solution computed by the densest mesh. It can be seen from **Fig. 9** that the tendencies of the errors stablize as the number of nodes on the crack increases, further verifying the mesh convergence of the models. The result demonstrates the capability of the hybrid SE/FE method to converge in modelling the nonlinear contact of cracks. For all the following numerical examples, we set the convergence threshold to an error of 2%.
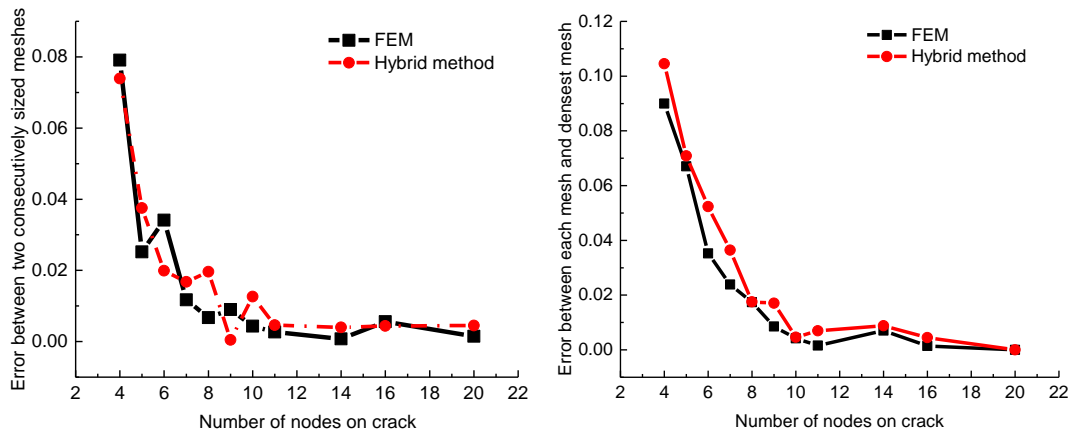

Fig. 9. Mesh convergence for the hybrid SE/FE model and the standard FE model of a cracked aluminum structure.

3.2. Second Harmonic Bulk Waves

Fig. 10 compares the time-domain and the frequency-domain signals obtained using the converged standard FE model and hybrid SE/FE model of the cracked structure shown in **Fig. 8**. It can be seen that the results obtained by the two different methods match very well, though there is a minor discrepancy in the amplitudes of the fundamental wave modes, which is most probably attributed to the use of different numerical integration schemes for the construction of stiffness matrices. The

frequency-domain signals confirm that the weak second harmonic wave modes could be modelled accurately using the hybrid method.
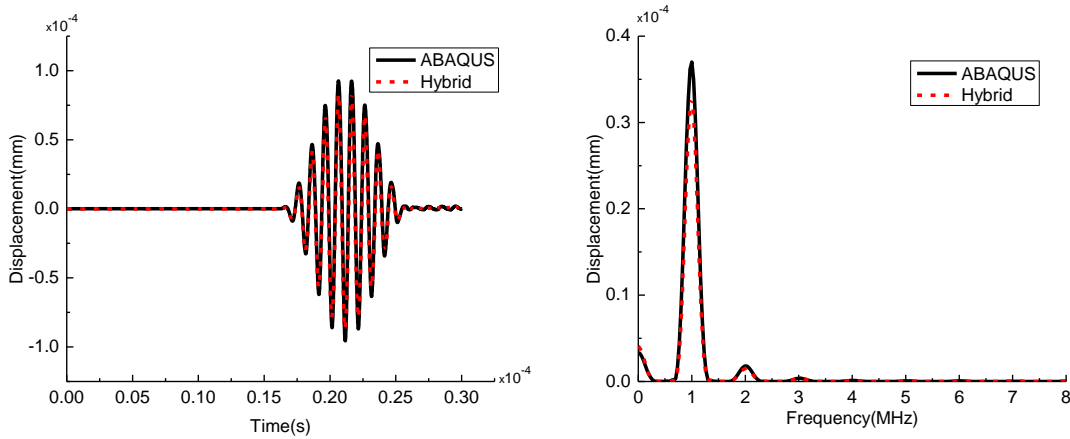

Fig. 10. Sensor signals computed by the standard FE model and the hybrid SE/FE model of a cracked aluminum structure.

The length and the orientation of a crack are of significant importance to structural integrity. The relationships between these crack characteristics and the nonlinear parameter are essentially the foundations of nonlinear ultrasonic inspection techniques. In using the hybrid SE/FE method to model cracks, the ratio between the number of FE nodes and the number of SE nodes (N_{FE}/N_{SE}) on a SE/FE interface would need to change with crack length and crack orientation due to convergence consideration. In order to minimize the numerical error introduced by mesh tying, $N_{FE}/N_{SE} \geq 2$ was maintained for all simulations [32].

As seen from **Fig. 11**, the nonlinear parameters and, more importantly, the trends of these parameters obtained using the two different methods demonstrate a high consistency. It is inferable that the SE/FE interface did not cause any disturbance to the propagation of both the fundamental and the second harmonic modes of longitudinal waves. Hence, it can be concluded that the hybrid SE/FE method is able to simulate a wide range of crack scenarios and can reach the same level of accuracy as the standard FEM. The numbers of DOFs employed by the hybrid SE/FE models and the standard FE models with cracks oriented at 90º are summarized in Table 1. It can be seen that the use of the hybrid method achieved an approximately 80% reduction. The numbers of the non-zero values in the lower triangles of the global stiffness matrices of the hybrid models and the standard FE models were also counted, as shown in Table 2. A reduction of approximately 40-50% was attained by the use of the hybrid method. The observation that the reduction in the number of non-zero values is not as significant as the reduction in the number of DOFs is attributed to fact that the global stiffness matrices of the hybrid models are denser than those of the standard FE models. Most importantly, as demonstrated in **Fig. 12**, the use of the hybrid method cut the computational time per time step by more than 50%. The computational time of the hybrid model with a 0.5 mm crack is slightly higher, because a denser mesh was used to accurately discretize

20

the relatively long crack and, hence, both the number of the DOFs of the model and the number of the non-zero values in the global stiffness matrix are larger.
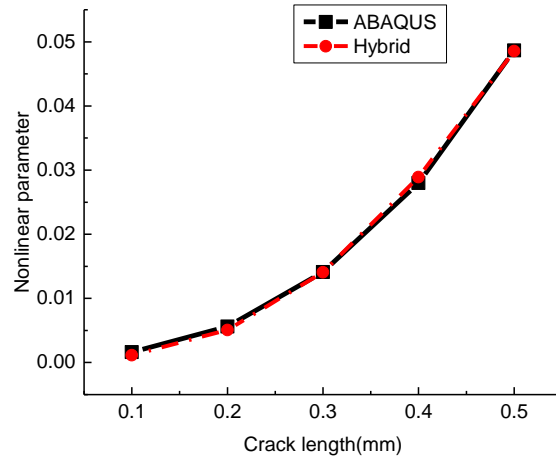
(a)
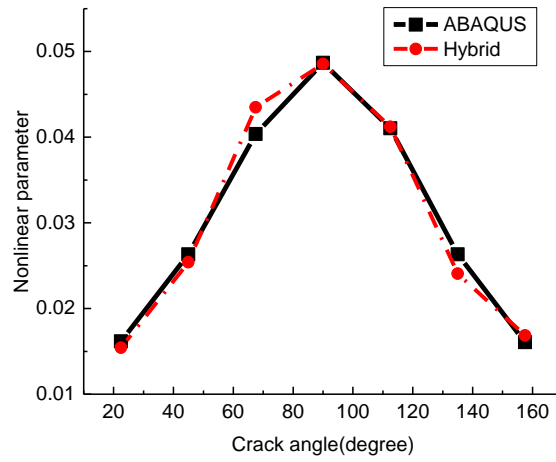
(b)

Fig. 11. Nonlinearity parameters computed by the standard FE model and the hybrid SE/FE model of a cracked aluminum structure at different (a) crack lengths and (b) crack orientations.

Table 1. Comparison of the numbers of DOFs in the hybrid SE/FE models and the standard FE models with 90° cracks of various lengths.

Crack length (mm)	0.1	0.2	0.3	0.4	0.5

Method					
FEM	86178	85889	85889	85817	85146
Hybrid	11605	11955	11377	11526	13132

Table 2. Comparison of the numbers of the non-zero values in lower triangles of the global stiffness matrices of the hybrid SE/FE models and the standard FE models with 90º cracks of various lengths.

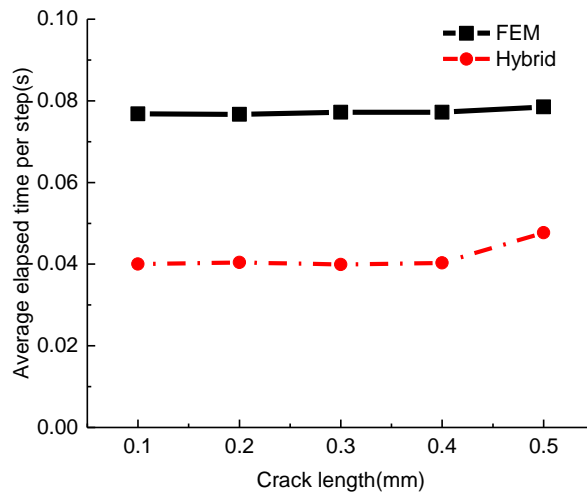| Crack length (mm) / Method	0.1	0.2	0.3	0.4	0.5
FEM	1617865	1617841	1613288	1615247	1627839
Hybrid	865399	871953	861067	863838	1022056

Fig. 12. Comparison of the mean computational times per time step of the hybrid SE/FE models and the standard FE models with 90º cracks of various lengths.

3.3. Collinear Mixing of Lamb Waves

We further applied the proposed hybrid method to simulating the collinear mixing of Lamb waves propagating in a thin plate with a crack. A 500mm×2mm domain, as shown in **Fig. 13**, was constructed, assuming plane strain. The material properties of the plate are same as those of the

cracked structure shown in **Fig. 8**. The crack is located in the center of the $2\text{mm} \times 2\text{mm}$ FE region and the rest of plate was discretized into SEs. Therefore, there are two straight interfaces between the two types of elements used. Two S0 Lamb waves were excited simultaneously at the one end of the plate in form of a transient dynamic pressure loading in the x-direction. The excitation signal takes the form of $F(t) = A_0[\sin(2\pi f_1 t) \times \sin(\pi f_1 t/N_1)^2 + \sin(2\pi f_2 t) \times \sin(\pi f_2 t/N_2)^2]$, where $f_1 = 450\,\text{kHz}$ and $f_2 = 600\,\text{kHz}$ are the central frequencies of the two Lamb waves excited, $N_1 = 30$ and $N_2 = 40$ are the number of the cycles of the two Lamb waves, and A_0 is the peak amplitude of the pressure loading. At a distance of 120 mm from the excitation point, the displacements in both the x- and the y-direction were acquired on the top surface of the structure.
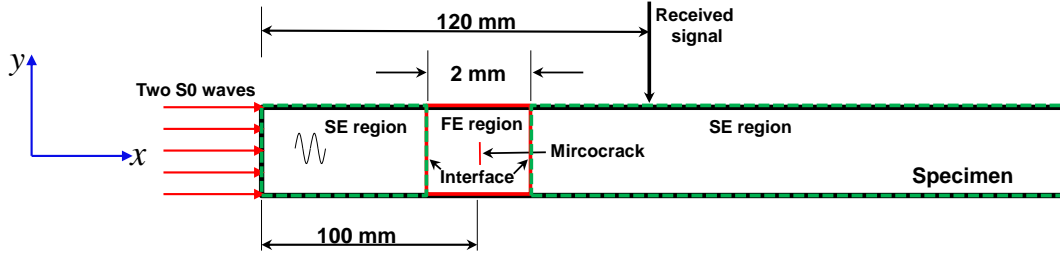

Fig. 13. Schematic diagram of the hybrid SE/FE model of a cracked aluminium plate that allows for the propagation of mix-frequency Lamb waves.

After examining mesh convergence for both hybrid and standard FEM executed by ABAQUS®, the size of the SEs of the model was set to 1.2 mm along x-direction and 2 mm along y-direction. The size of the FEs varied with the length of the crack, e.g. 0.0167 mm elements were used for a 0.1 mm crack and 0.0417 mm elements for a 0.5 mm crack. The stable time increment was set to 0.1 ns. For mix-frequency wave modes [59-61], the nonlinear parameters for the sum-frequency and the difference-frequency waves are given by $\beta_{sum} = A_{sum}/(A_1 A_2)$ and $\beta_{diff} = A_{diff}/(A_1 A_2)$ respectively, where A_1 and A_2 denote the amplitudes of two fundamental wave modes excited, and A_{sum} and A_{diff} the amplitudes of the sum-frequency and the difference-frequency wave modes.(b)

Fig. 14 shows the time-domain and the frequency-domain sensor signals in the x- and the y-directions, obtained using the standard FE model and the hybrid SE/FE model. It is seen that both difference-frequency and sum-frequency wave modes were generated, in both directions too. By comparing the signals computed by the two different methods, it is observed that a good agreement is achieved in both the time-domain and the frequency-domain and in both directions. In the x-direction, the amplitude of the difference-frequency wave mode is higher than that of the sum-frequency wave mode, while the trend is the opposite in the y-direction.
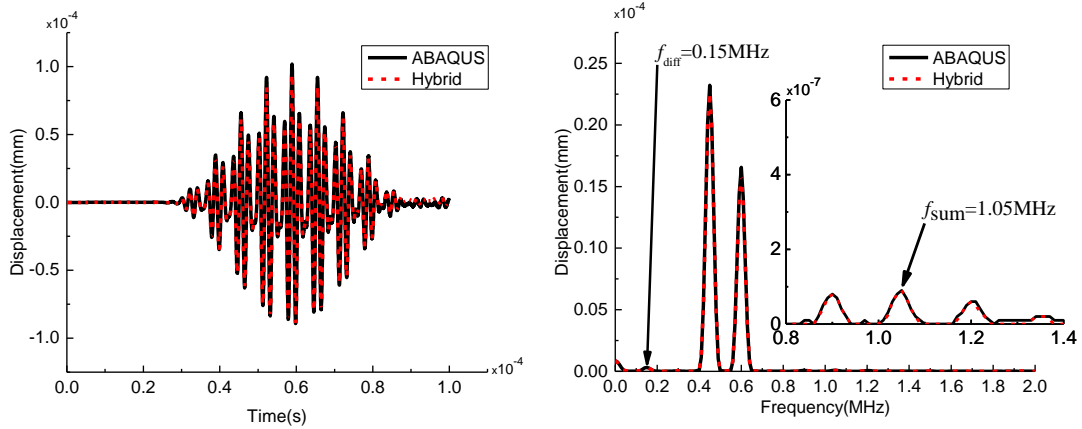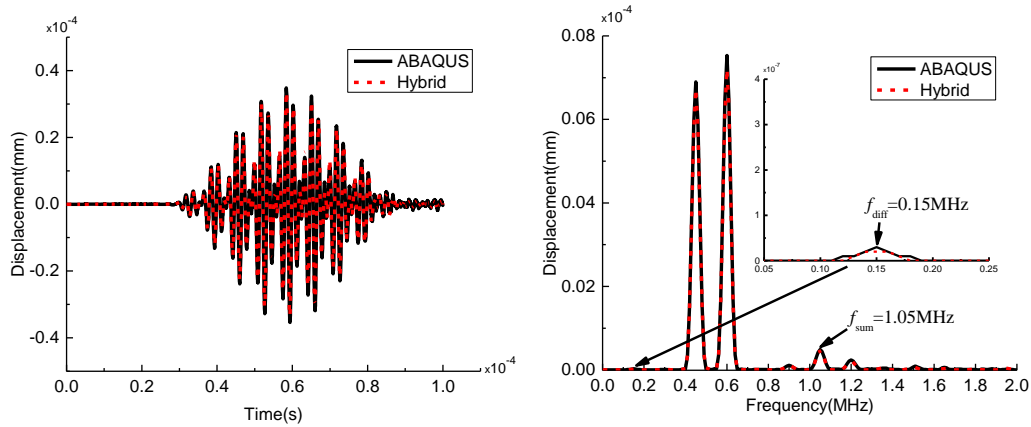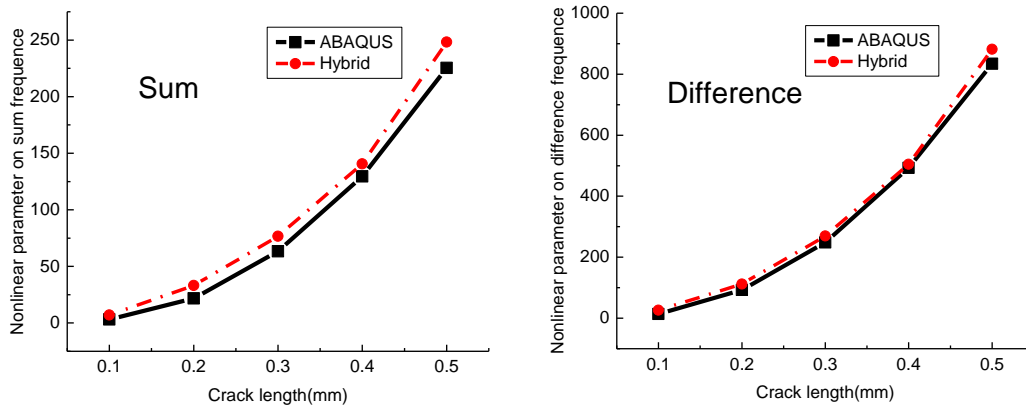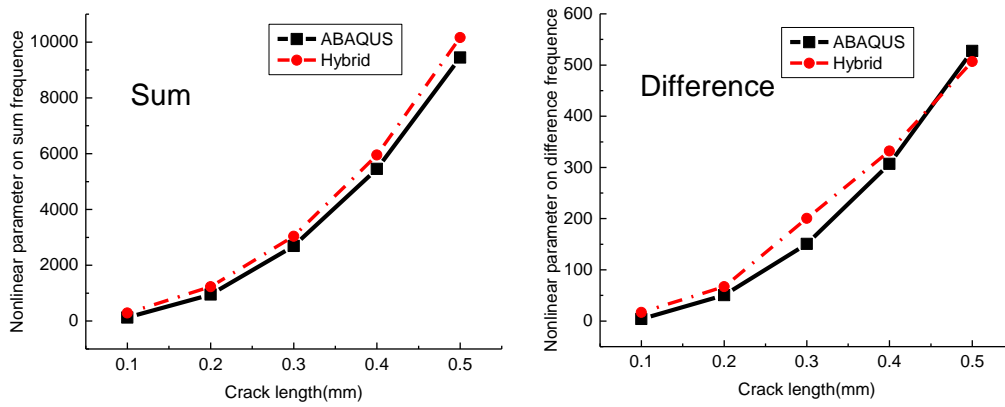
Fig. 14. (a) x-direction and (b) y-direction sensor signals computed by the standard FE model and the hybrid SE/FE model of a cracked aluminum plate.

Fig. 15 presents the relationships between the nonlinear parameter and the crack length, obtained using the standard FE model and the hybrid SE/FE model. Understandably, the nonlinear parameters related to both the difference-frequency and the sum-frequency wave modes in both the x- and the y-directions increase monotonically with crack length. Although there is a minor discrepancy between the results obtained by the two different methods, the tendencies are exactly the same.

Fig. 15. Nonlinearity parameters related to (a) the x-direction and (b) the y-direction sensor signals, computed by the standard FE model and the hybrid SE/FE model of a cracked aluminum plate.

The results presented in this section further indicates that the proposed hybrid method is able reach a good accuracy and stability for simulating nonlinear ultrasonic wave modes induced by the nonlinear contact of crack surfaces. The SE/FE interfaces allowed for the flow of energy between the two types of meshes. Hence, there is little difference between the results obtained using the hybrid method and the standard FEM. As shown in Table 3, the hybrid SE/FE model achieved a significant reduction in total number of DOFs, compared to the standard FE model.

Table 3. Comparison of the numbers of DOFs in the hybrid SE/FE models and the standard FE models with cracks of various lengths.

Crack length (mm) / Method	0.1	0.2	0.3	0.4	0.5
FEM	445246	455850	455854	477060	477064
Hybrid	6836	6628	6628	6478	6516

3.4. Non-Collinear Mixing of Bulk Waves

Non-collinear mixing of ultrasonic waves [62-64] is a relatively new concept and has become a research hotspot due to some of its special merits such as the possibility of locating defects in certain types of structures and a diverse range of usable excitation frequencies. To implement the non-collinear mixing of ultrasonic waves in a structure, two fundamental waves are excited separately and propagated in the structure. When the two waves encounter at the position of interest at an angle ϕ, they combine into a new wave mode which propagates in a new direction, as shown in **Fig. 16**.
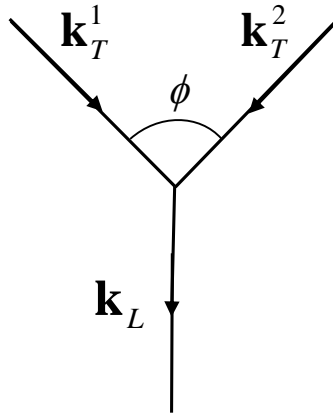

Fig. 16. Schematic diagram for the mixing of two fundamental waves ($\mathbf{k}_T^1$ and $\mathbf{k}_T^2$) which results in a third wave ($\mathbf{k}_L$).

The propagation directions of the two fundamental excitation waves, which are essentially determined by their polarization directions, should be pre-determined, because they dictate whether the third, mixing wave mode will be generated. For classical material nonlinearity, the generation of the new mixing wave mode replies on the fulfillment of the following resonance condition [63] which is derived from the nonlinear wave theory

$$\cos\phi = \frac{c_T^2}{c_L^2} + \frac{1}{2}(\frac{c_T^2}{c_L^2}-1)(\frac{f_1}{f_2}+\frac{f_2}{f_1})$$

(39)

26

where c_T and c_L are the velocities of the transverse and the longitudinal waves in the medium, f_1 and f_2 are frequencies of the fundamental excitation waves. However, the resonance condition would not be necessary if contact nonlinearity is considered [62]. In this case, the mixing wave mode would be generated as long as the two fundamental excitation waves meet at the position where the contact nonlinearity is present.

Delamination is a common type of defect that would exist at the interface of two different types of materials. It has become a serious concern nowadays due to the increase use of composite laminates and 3D-printed materials. The contact mechanics of delamination is highly similar to that of cracks. In this respect, the non-collinear mixing method could be an effective approach for detecting delamination.

In this work, the collinear mixing of two ultrasonic bulk waves at a delamination site was simulated by the hybrid SE/FE approach. **Fig. 17** shows a $200\text{mm} \times 100\text{mm}$ bimetal structure that is divided into two parts by the centerline in the thickness direction. The upper half of the structure is made of aluminum and the lower half steel. A 2 mm long delamination is located at the center of the structure at the interface between the two metals. Two glass wedges are placed on the top surface of the structure, symmetric about the y-axis. It is assumed that both the interfaces between the glass wedges and the aluminum region, and the interface between the aluminum and the steel regions, except for the delamination site, are perfectly bonded. The square region surrounding the delamination ($L = 4$ mm) was meshed by FEs, and the remaining part of the structure was discretized into SEs. The material properties of the different constituents of the structure are given in Table 4.
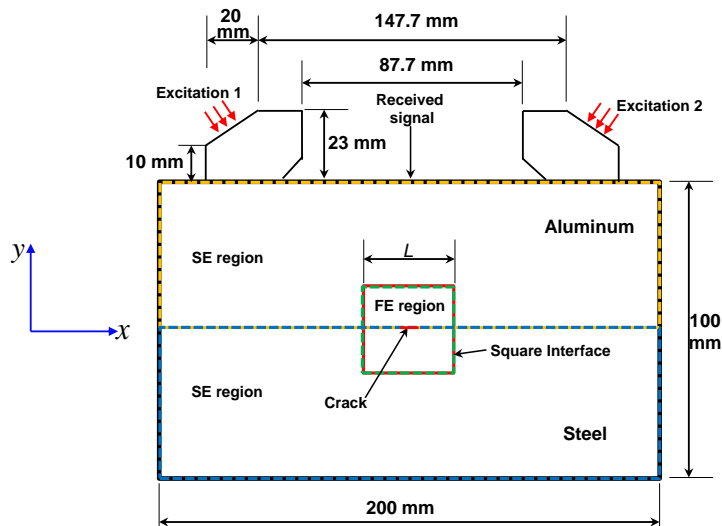

Fig. 17. Schematic diagram of the hybrid SE/FE model of a bimetal structure with a crack that allows for the collinear mixing of bulk waves.

Table 4. Material properties of a bimetal structure with a crack.

Property Material	Young's modulus (GPa)	Poisson's ratio	Density ($kg \cdot m^{-3}$)
Aluminum	70	0.33	2700
Steel	200	0.33	7600
Glass	4	0.35	1180

Two longitudinal waves with central frequencies of 1.5 MHz and 2 MHz were loaded onto the wedges. The longitudinal waves were converted into shear waves when they obliquely passed through the interfaces between the glass wedges and the aluminum. The wedges are designed to control the mixing location of the fundamental incident waves based on the resonance condition shown in Eq. (39). The shear waves then propagated into the structure and when they met at the delamination site, a third longitudinal wave mode, which presented itself as the sum-frequency mode of the two fundamental incident waves, was generated. Sensor signals were acquired at the center of top surface of the structure. After carrying out a mesh convergence study, the maximum size of the SEs for the glass wedges was set to 0.5 mm, and that of the SEs for the aluminum and the steel regions was set to 1 mm. The element size of the FEs for the delamination region was set 0.05 mm. The stable time increment for the simulation was set to $1 \times 10^{-10} s$. The results obtained by the hybrid SE/FE method was also validated by the standard FEM executed by ABAQUS®.

Fig. 18 shows the sum-frequency wave modes, obtained by the hybrid FE/SE model and the standard FE model of the bimetal structure with a crack, in the time-domain and in the frequency-domain. It is worth mentioning that the frequency-domain sensor signals are the Fourier transforms of the second wave packets of the signals. The agreement between the results obtained by the two different methods is very good, reinstating that FE/SE interfaces do not introduce any distortion. Moreover, the number of DOFs employed by the standard FE model is 5,080,720, while that employed by the hybrid model is only 532,660. The numbers of the non-zero values in the lower triangles of the global stiffness matrices of the two models are 96,468,028 (FE) and 38,416,180 (hybrid). The mean computational times per time step of the models are 4.4933s (FE) and 1.5959s (hybrid). In fact, the larger the structure to be modelled is, the higher the saving in computational expense to be achieved by the hybrid method would be. The time-domain signal of the sum-frequency wave mode that would be acquired from the bimetal structure if there was no delamination was computed by the standard FEM and is shown in **Fig. 19**. The signal is essentially noise, as evident through its amplitude, meaning that there would not be any mixing wave mode generated if there was no defect.
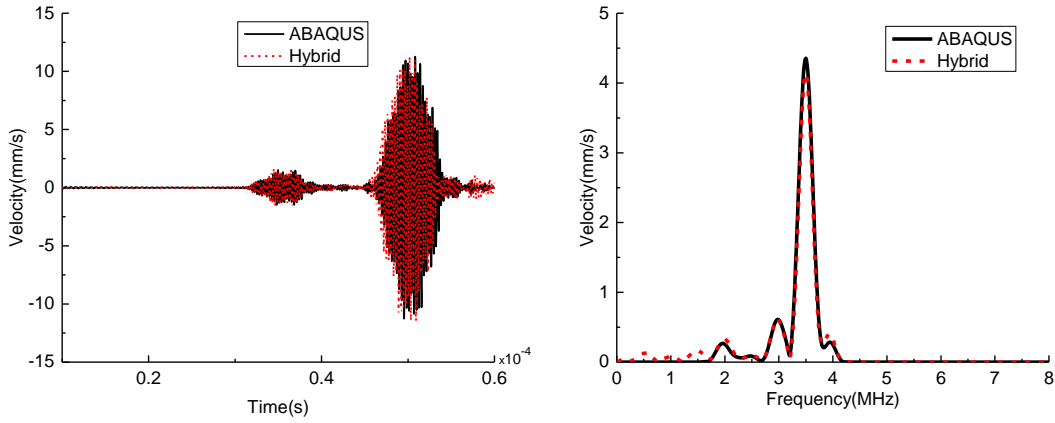
Fig. 18. Sum-frequency wave modes computed by the standard FE model and the hybrid SE/FE model of the bimetal structure with a crack.
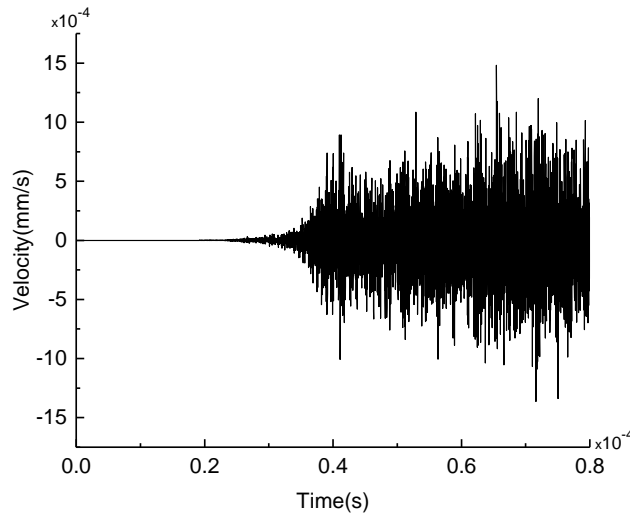

Fig. 19. Sum-frequency wave mode computed by the standard FE model of the bimetal structure without a crack.

When the two fundamental shear waves met at the delamination site, both their reflected and transmitted components generated a sum-frequency wave mode, one propagating towards the top surface of the structure along the $-(\mathbf{k}_T^1 + \mathbf{k}_T^2)$ direction, and the other towards the bottom surface of the structure along the $\mathbf{k}_T^1 + \mathbf{k}_T^2$ direction. The first wave packet in the time-domain signal essentailly represents the sum-frequency wave mode that was resulted from the reflected components of the two shear waves. When the transmitted sum-frequency wave mode reached the bottom surface of the structure, it was reflected towards the top surface, presenting itself as the second wave packet in the time-domain signal. Due to the relatively small size of the delamination, the transmitted components of two shear waves were much more dominant than their reflected

components. This explains why the reflected sum-frequency wave mode was much weaker than its transmitted counterpart. From the frequency-domain signals showed in **Fig. 18**, it is seen that the frequency of the transmitted sum-frequency wave mode is equal to 3.5 MHz, which is the sum of the frequencies of the two fundamental shear waves.

4. Conclusion

In this paper, a 2D hybrid SE/FE method for numerically approximating the generation and propagation of crack-induced nonlinear ultrasonic wave modes in solid structures is proposed. While pure SEM can reduce the number of DOFs in a system and achieve a high accuracy, the discretization of a small crack into SEs would result in a large number of nodes that are overly close to each other around the crack, leading to a large computational cost and potential loss of computational stability. On the other hand, such difficulties in discretizing complex geometric features can be overcome by the use of the standard low-order FEM. Nevertheless, the FEM requires much more computational resources than the SEM. The proposed hybrid method, by taking advantage of both worlds, is able to deal with irregular geometries and, at the same time, consumes low computational effort.

In using the proposed method, SE and FE regions, which employ shape functions of different orders, are tied by the surface-to-surface approach that is enabled by the Lagrange multipliers method. Cracks are formulated as frictionless contact by the surface-to-surface contact strategy and regulated by a penalty method. The transient responses of systems are solved by explicit time integration.

Mesh convergence studies were carried out. For linear elastic structures, the standard FEM with 4-node quadrilateral elements requires around 45 nodes per wavelength to reach convergence, whereas the SEM with 25-node GLL elements requires only 9 nodes per wavelength, when convergence threshold was set to 2%. For a structure with a crack, mesh convergence was achieved by further reducing the size of the FEs for meshing the crack beyond the convergence criterion for wave propagation. It is shown that the coupling of different types of elements does not influence convergence. It is worth mentioning that mesh convergence should be done for every model with cracks because both crack length and excitation frequency would affect mesh convergence. Then, three numerical experiments were conducted to demonstrate the feasibility of the hybrid SE/FE method in solving nonlinear contact problems. Accurate numerical solutions were obtained for the generation of the second harmonic mode of bulk waves, the collinear mixing of Lamb waves in a thin plate, and the non-collinear mixing of bulk waves in a bimetal structure. The outstanding agreements between the results computed by the hybrid method, realized using an inhouse code, and those obtained by the standard FEM, executed by both inhouse code and the commercial software package ABAQUS®, further indicate capability of the hybrid method in addressing various large-scale and complicated realistic engineering structures.

More than anything, as demonstrated by the mesh convergence studies and the numerical experiments, the use of the proposed hybrid SE/FE method tremendously reduces the DOFs in

systems, the numbers of the non-zero values in global stiffness matrices, and computation times. The hybrid method would be particularly advantageous when dealing with large-scale simulations as it could dramatically ease the demand on memory usage. Through this work, the hybrid method has been shown to be a highly competitive alternative method for studying various crack-induced nonlinear ultrasonic wave modes that are of significant importance to the development of nonlinear ultrasonic inspection techniques.

Acknowledgment

References

1. Halabe, U.B. and R. Franklin, *Fatigue crack detection in metallic members using ultrasonic Rayleigh waves with time and frequency analyses.* Materials Evaluation, 2001. **59**(3): p. 424-431.

2. Kerbrat, E., et al., *Ultrasonic nondestructive testing of scattering media using the decomposition of the time-reversal operator.* Ieee Transactions on Ultrasonics Ferroelectrics and Frequency Control, 2002. **49**(8): p. 1103-1113.

3. Monchalin, J.P., et al., *Detection of flaws in materials by laser-ultrasonics.* Iutam Symposium on Advanced Optical Methods and Applications in Solid Mechanics, 2000. **82**: p. 437-450.

4. Li, W., Y. Cho, and J.D. Achenbach, *Detection of thermal fatigue in composites by second harmonic Lamb waves.* Smart Materials and Structures, 2012. **21**(8).

5. Matlack, K.H., et al., *Experimental characterization of efficient second harmonic generation of Lamb wave modes in a nonlinear elastic isotropic plate.* Journal of Applied Physics, 2011. **109**(1).

6. Wang, L.H.V., *Mechanisms of ultrasonic modulation of multiply scattered coherent light: An analytic model.* Physical Review Letters, 2001. **87**(4).

7. Puso, M.A. and T.A. Laursen, *A mortar segment-to-segment contact method for large deformation solid mechanics.* Computer Methods in Applied Mechanics and Engineering, 2004. **193**(6-8): p. 601-629.

8. McDevitt, T.W. and T.A. Laursen, *A mortar-finite element formulation for frictional contact problems.* International Journal for Numerical Methods in Engineering, 2000. **48**(10): p. 1525-1547.

9. Hallquist, J.O., G.L. Goudreau, and D.J. Benson, *Sliding Interfaces with Contact-Impact in Large-Scale Lagrangian Computations.* Computer Methods in Applied Mechanics and Engineering, 1985. **51**(1-3): p. 107-137.

10. Yelve, N.P., M. Mitra, and P.M. Mujumdar, *Higher harmonics induced in lamb wave due to partial debonding of piezoelectric wafer transducers.* Ndt & E International, 2014. **63**: p. 21-27.

11.   Guha, A. and C.R. Bijudas, *Higher and Sub-harmonic Lamb wave mode generation due to debond-induced contact nonlinearity.* Health Monitoring of Structural and Biological Systems 2016, 2016. **9805**.

12.   Li, F.L., et al., *Mixing of ultrasonic Lamb waves in thin plates with quadratic nonlinearity.* Ultrasonics, 2018. **87**: p. 33-43.

13.   Bathe, K.-J.r. and K.-J.r. Bathe, *Finite element procedures*. 1996, Englewood Cliffs, N.J.: Prentice Hall. xiv, 1037 p.

14.   Reddy, J.N., *An introduction to nonlinear finite element analysis*. 2004, Oxford ; New York: Oxford University Press. xv, 463 p.

15.   Harari, I., *A survey of finite element methods for time-harmonic acoustics.* Computer Methods in Applied Mechanics and Engineering, 2006. **195**(13-16): p. 1594-1607.

16.   Idesman, A.V., M. Schmidt, and J.R. Foley, *Accurate finite element modeling of linear elastodynamics problems with the reduced dispersion error.* Computational Mechanics, 2011. **47**(5): p. 555-572.

17.   Cherukuri, H.P., *Dispersion analysis of numerical approximations to plane wave motions in an isotropic elastic solid.* Computational Mechanics, 2000. **25**(4): p. 317-328.

18.   Ihlenburg, F. and I. Babuska, *Finite-Element Solution of the Helmholtz-Equation with High Wave-Number .1. The H-Version of the Fem.* Computers & Mathematics with Applications, 1995. **30**(9): p. 9-37.

19.   Komatitsch, D. and J. Tromp, *Introduction to the spectral element method for three-dimensional seismic wave propagation.* Geophysical Journal International, 1999. **139**(3): p. 806-822.

20.   Patera, A.T., *A Spectral Element Method for Fluid-Dynamics - Laminar-Flow in a Channel Expansion.* Journal of Computational Physics, 1984. **54**(3): p. 468-488.

21.   De Frutos, J. and J. Novo, *A spectral element method for the Navier-Stokes equations with improved accuracy.* Siam Journal on Numerical Analysis, 2000. **38**(3): p. 799-819.

22.   Ostachowicz, W.M., *Guided waves in structures for SHM : the time-domain spectral element method*. 2012, Chichester, West Sussex ; Hoboken, NJ: Wiley. xii, 337 p.

23.   Peng, H.K., G. Meng, and F.C. Li, *Modeling of wave propagation in plate structures using three-dimensional spectral element method for damage detection.* Journal of Sound and Vibration, 2009. **320**(4-5): p. 942-954.

24.   Kudela, P., M. Krawczuk, and W. Ostachowicz, *Wave propagation modelling in 1D structures using spectral finite elements.* Journal of Sound and Vibration, 2007. **300**(1-2): p. 88-100.

25.   Ramabathiran, A.A. and S. Gopalakrishnan, *Time and Frequency Domain Finite Element Models for Axial Wave Analysis in Hyperelastic Rods.* Mechanics of Advanced Materials and Structures, 2012. **19**(1-3): p. 79-99.

26.   Kudela, P., *Parallel implementation of spectral element method for Lamb wave propagation modeling.* International Journal for Numerical Methods in Engineering, 2016. **106**(6): p. 413-429.

27.	Kudela, P., J. Moll, and P. Fiborek, *Parallel spectral element method for guided wave based structural health monitoring.* Smart Materials and Structures, 2020. **29**(9).

28.	Carpenter, N.J., R.L. Taylor, and M.G. Katona, *Lagrange Constraints for Transient Finite-Element Surface-Contact.* International Journal for Numerical Methods in Engineering, 1991. **32**(1): p. 103-128.

29.	Mokhtar, M.A., A.K. Darpe, and K. Gupta, *Investigations on bending-torsional vibrations of rotor during rotor-stator rub using Lagrange multiplier method.* Journal of Sound and Vibration, 2017. **401**: p. 94-113.

30.	Brun, M., et al., *External coupling software based on macro- and micro-time scales for explicit/implicit multi-time-step co-computations in structural dynamics.* Finite Elements in Analysis and Design, 2014. **86**: p. 101-119.

31.	Verkaik, A.C., et al., *An overlapping domain technique coupling spectral and finite elements for fluid-structure interaction.* Computers & Fluids, 2015. **123**: p. 235-245.

32.	Casadei, F., et al., *A mortar spectral/finite element method for complex 2D and 3D elastodynamic problems.* Computer Methods in Applied Mechanics and Engineering, 2002. **191**(45): p. 5119-5148.

33.	Bernardi, C. and N. Chorfi, *Mortar spectral element methods for elliptic equations with discontinuous coefficients.* Mathematical Models & Methods in Applied Sciences, 2002. **12**(4): p. 497-524.

34.	Zuchowski, L., M. Brun, and F. De Martin, *Co-simulation coupling spectral/finite elements for 3D soil/structure interaction problems.* Comptes Rendus Mecanique, 2018. **346**(5): p. 408-422.

35.	Fiborek, P., P. Kudela, and W.M. Ostachowicz, *2D-3D interface coupling in the time domain spectral element method for the adhesive layer effects on guided wave propagation in composite plates.* Smart Materials and Structures, 2019. **28**(5).

36.	Duczek, S., A.A. Saputra, and H. Gravenkamp, *High order transition elements: The xNy-element concept-Part I: Statics.* Computer Methods in Applied Mechanics and Engineering, 2020. **362**.

37.	Xiao, S.P. and T. Belytschko, *A bridging domain method for coupling continua with molecular dynamics.* Computer Methods in Applied Mechanics and Engineering, 2004. **193**(17-20): p. 1645-1669.

38.	Elleithy, W.M. and H.J. Al-Gahtani, *An overlapping domain decomposition approach for coupling the finite and boundary element methods.* Engineering Analysis with Boundary Elements, 2000. **24**(5): p. 391-398.

39.	Rethore, J., A. Gravouil, and A. Combescure, *An energy-conserving scheme for dynamic crack growth using the eXtended finite element method.* International Journal for Numerical Methods in Engineering, 2005. **63**(5): p. 631-659.

40.	Starc, B., G. Cepon, and M. Boltezar, *A mixed-contact formulation for a dynamics simulation of flexible systems: An integration with model-reduction techniques.* Journal of Sound and Vibration, 2017. **393**: p. 145-156.

41.	Simulia, D., *Abaqus (2018) User's Manual.* Provid RI, USA DS SIMULIA Corp, 2018.

42.	Blanloeuil, P., et al., *Time reversal invariance for a nonlinear scatterer exhibiting contact acoustic nonlinearity.* Journal of Sound and Vibration, 2018. **417**: p. 413-431.

43.	Dolbow, J., N. Moes, and T. Belytschko, *An extended finite element method for modeling crack growth with frictional contact.* Computer Methods in Applied Mechanics and Engineering, 2001. **190**(51-52): p. 6825-6846.

44.	Semperlotti, F., K.W. Wang, and E.C. Smith, *Localization of a breathing crack using nonlinear subharmonic response signals.* Applied Physics Letters, 2009. **95**(25).

45.	Puso, M.A., *A 3D mortar method for solid mechanics.* International Journal for Numerical Methods in Engineering, 2004. **59**(3): p. 315-336.

46.	Zienkiewicz, O.C., R.L. Taylor, and D. Fox, *The finite element method for solid and structural mechanics.* 7th ed. 2014, Amsterdam ; Boston: Elsevier/Butterworth-Heinemann. xxxi, 624 pages.

47.	Puso, M.A., T.A. Laursen, and J. Solberg, *A segment-to-segment mortar contact method for quadratic elements and large deformations.* Computer Methods in Applied Mechanics and Engineering, 2008. **197**(6-8): p. 555-566.

48.	Laursen, T.A., M.A. Puso, and J. Sanders, *Mortar contact formulations for deformable-deformable contact: Past contributions and new extensions for enriched and embedded interface formulations.* Computer Methods in Applied Mechanics and Engineering, 2012. **205**: p. 3-15.

49.	Ehrl, A., et al., *A dual mortar approach for mesh tying within a variational multiscale method for incompressible flow.* International Journal for Numerical Methods in Fluids, 2014. **76**(1): p. 1-27.

50.	Spreiter, Q. and M. Walter, *Classical molecular dynamics simulation with the Velocity Verlet algorithm at strong external magnetic fields.* Journal of Computational Physics, 1999. **152**(1): p. 102-119.

51.	Popp, A., et al., *A dual mortar approach for 3D finite deformation contact with consistent linearization.* International Journal for Numerical Methods in Engineering, 2010. **83**(11): p. 1428-1465.

52.	Konyukhov, A. and R. Izi, *Introduction to computational contact mechanics : a geometrical approach*, in *Wiley series in computational mechanics*. 2015, Wiley,: Chichester, West Sussex. p. 1 online resource.

53.	Yang, B., T.A. Laursen, and X.N. Meng, *Two dimensional mortar contact methods for large deformation frictional sliding.* International Journal for Numerical Methods in Engineering, 2005. **62**(9): p. 1183-1225.

54.	Lyubchanskii, I.L., et al., *Second-harmonic generation from realistic film-substrate interfaces: The effects of strain.* Applied Physics Letters, 2000. **76**(14): p. 1848-1850.

55.	Matlack, K.H., et al., *Review of Second Harmonic Generation Measurement Techniques for Material State Determination in Metals.* Journal of Nondestructive Evaluation, 2015. **34**(1).

56.   Awatani, T., et al., *Second harmonic generation study on electrochemical deposition of palladium on a polycrystalline gold electrode.* Journal of Electroanalytical Chemistry, 2002. **524**: p. 184-193.

57.   Zhu, W.J., et al., *Modeling of ultrasonic nonlinearities for dislocation evolution in plastically deformed materials: Simulation and experimental validation.* Ultrasonics, 2016. **68**: p. 134-141.

58.   Lee, T.H. and K.Y. Jhang, *Experimental investigation of nonlinear acoustic effect at crack.* Ndt & E International, 2009. **42**(8): p. 757-764.

59.   Sohn, H., et al., *Nonlinear ultrasonic wave modulation for online fatigue crack detection.* Journal of Sound and Vibration, 2014. **333**(5): p. 1473-1484.

60.   Donskoy, D., A. Sutin, and A. Ekimov, *Nonlinear acoustic interaction on contact interfaces and its use for nondestructive testing.* Ndt & E International, 2001. **34**(4): p. 231-238.

61.   Duffour, P., M. Morbidini, and P. Cawley, *A study of the vibro-acoustic modulation technique for the detection of cracks in metals.* Journal of the Acoustical Society of America, 2006. **119**(3): p. 1463-1475.

62.   Blanloeuil, P., A. Meziane, and C. Bacon, *2D finite element modeling of the non-collinear mixing method for detection and characterization of closed cracks.* Ndt & E International, 2015. **76**: p. 43-51.

63.   Ishii, Y., S. Biwa, and T. Adachi, *Non-collinear interaction of guided elastic waves in an isotropic plate.* Journal of Sound and Vibration, 2018. **419**: p. 390-404.

64.   Rose, L.R.F., et al., *Analytical and numerical modelling of non-collinear wave mixing at a contact interface.* Journal of Sound and Vibration, 2020. **468**.